Theoretical and Applied Fracture Mechanics 112 (2021) 102904

Contents lists available at ScienceDirect

Theoretical and Applied Fracture Mechanics

journal homepage: www.elsevier.com/locate/tafmec

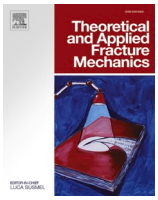

Mode I stress intensity factors for semi-elliptical fatigue cracks in curved round bars

Mads Aursand *, Bjørn H. Skallerud

Norwegian University of Science and Technology (NTNU), Department of Structural Engineering, Richard Birkelandsvei 1A, 7491 Trondheim, Norway

ARTICLE INFO

Keywords:
Stress intensity factor (SIF)
Semi-elliptical surface crack
Curved round bar
Fatigue crack growth

ABSTRACT

Some cyclically loaded components such as mooring chains can develop fatigue cracks in locations where the shape of the part is equivalent to that of a curved or bent round bar. Here we consider a semi-elliptical crack growing from the surface of a curved round bar. This geometry can for example represent a chain link segment with a crack located at its inner- or outer radius. The surface crack can be either almond shaped, sickle shaped or straight-fronted. Stress intensity factors (SIFs) over the fronts of such crack geometries are in the present work investigated for several elementary mode I stress distributions. Finite element analysis and linear elastic fracture mechanics methods are used to develop semi-analytical solutions for the SIF at any point on the crack front. Effects of relative bar curvature on numerical results are demonstrated. Relative to otherwise identical cracks in straight bars, SIFs for cracks in the curved bars considered here are found to differ by up to 8%. With an offshore mooring chain model as a case example, the estimation of SIFs for cracks in a complex residual stress field is furthermore demonstrated using a cubic polynomial stress approximation.

1. Introduction

Predicting the remaining fatigue life of a round bar component containing a surface crack is a well-known engineering problem that is relevant to a vast range of different industries. A semi-elliptical crack model is often used to represent such cracks, allowing a wide range of crack shapes to be approximated using no more than two parameters. Fatigue in metallic materials under high-cycle fatigue conditions will furthermore usually only involve plasticity at a small-scale. Crack growth analysis methods based on linear elastic fracture mechanics can therefore often be considered acceptable. In many cases, the round bar component containing the crack will be a straight cylindrical bar subjected to tension and/or bending loads. Examples of such cases are cracks in rods and shafts. In certain cases, the crack under consideration is on the other hand growing in a distinctly curved or bent round bar component. Compared to the simpler case of a straight bar, the analysis of cracks growing in curved bars does however not appear to have received much attention in published literature.

A relevant example problem involving cracks in curved round bars can be found when considering fatigue crack growth in offshore mooring chains. Chains of this type are frequently used for anchoring oil and gas installations in conditions where corrosion fatigue can be an important damage mechanism. Fatigue cracks in mooring chains are in most cases observed to grow from the exterior and interior sides of the curved parts of the links [1–3]. Fig. 1 indicates the two most common fatigue crack locations. The stress distributions present in these regions of the link will generally have a non-trivial relationship with the remote tension load P, and can often not be adequately described by simply superimposing a uniform tensile stress and a linear bending stress [4,5]. In addition to the possible influence of bar curvature by itself, it may thus also become necessary to consider a relatively complex loading of the crack.

Semi-elliptical surface cracks in round bars can broadly be classified into three distinct shape categories. If the crack area is convex, the crack can be described as almond shaped. If the crack area on the other hand is concave, the crack can be described as sickle shaped. The third category is the straight-fronted crack, which is a special case of the two former elliptical shapes and can serve as an intermediate shape in between them. Based on empirical observations, fatigue cracks in smooth round bars subjected to cyclic tension or bending loads generally tend to be almond shaped. Sickle shaped cracks can however also be encountered in some cases, for example when a crack is growing from a circumferential notch or similar stress concentration [6]. Since offshore mooring chains often develop notable stress concentrations due to corrosion and wear [7], all three crack shape categories could potentially be relevant. And since the bar diameter in this application often exceeds 100 mm, it

* Corresponding author.
E-mail address: mads.aursand@ntnu.no (M. Aursand).

https://doi.org/10.1016/j.tafmec.2021.102904
Received 7 October 2020; Received in revised form 16 December 2020; Accepted 4 January 2021
Available online 7 January 2021

Nomenclature

$A_{i,qrs}$	coefficients for polynomial geometry correction factor solutions (crack center)
a	crack depth
a_{elp}, b_{elp}	ellipse semi-axes
$B_{i,qrs}$	coefficients for polynomial geometry correction factor solutions (crack edge)
$C_{i,qrst}$	coefficients for polynomial geometry correction factor solutions (crack front)
D	bar diameter
F_i	geometry correction factor for reference stress σ_i
FEA	finite element analysis
K_I	stress intensity factor, mode I loading
ΔK	stress intensity factor range (K_{max} - K_{min})
ΔK_{eff}	effective stress intensity factor range ($U^*\Delta K$)
N	number of fatigue cycles
R_C	bar radius of curvature
SIF	stress intensity factor
U	effective stress intensity factor ratio ($\Delta K_{eff}/\Delta K$)
α	crack shape parameter
β	relative crack depth
γ	bar curvature parameter
ν	Poisson's ratio
ξ	relative crack front position
σ_i	reference stresses for polynomial stress distribution ($i = 0$, 1, …, 6)
σ_z	normal stress in crack plane

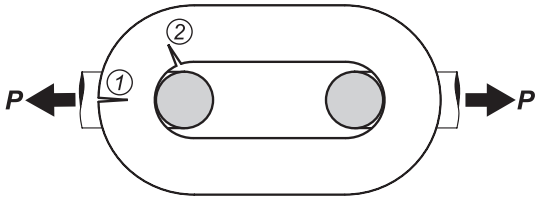

Fig. 1. Offshore mooring chain link. Typical fatigue crack locations (1 and 2) are indicated.

can also be added that the size of the fatigue crack under consideration sometimes can be rather small relative to the diameter.

In order to model the growth of a semi-elliptical fatigue crack as a linear elastic fracture mechanics problem, the stress intensity factor (SIF) associated with the crack front must be evaluated. This allows crack growth rates under constant amplitude loading to be calculated by correlating the cyclic stress intensity factor range (ΔK) with experimentally determined crack growth rates. Additionally, a method for predicting crack shape development will be needed. One approach can be to assume that changes in crack aspect ratio must be driven by a variation in local crack growth rates over the crack front. When crack growth rates are calculated from ΔK, this does however require evaluation of SIFs at multiple different crack front locations.

The evaluation of SIFs associated with almond shaped cracks in straight round bars under tension and bending loads is a subject that has been addressed in a number of publications [8–12]. A review covering various SIF solutions for this geometry has been presented by Toribio et al. [13]. In addition, the evaluation of SIFs for almond shaped cracks in curved round bars has to some extent been addressed by the present authors [5]. The subject of calculating SIFs associated with sickle shaped cracks has been addressed in a handful of publications [14–17]. Only a few of the various closed-form solutions found in literature do however readily allow for SIFs to be evaluated at arbitrary crack front positions. Solutions addressing both almond- and sickle shaped cracks in curved round bars furthermore appear to be hard to find.

The main subject of the present paper is the evaluation of SIFs associated with semi-elliptical cracks in curved round bars subjected to mode I loading. With bar curvature considered as an independent variable, semi-analytical polynomial solutions for approximating the SIF variation over almond- and sickle shaped crack fronts are hereafter developed. Effect of bar curvature on SIFs and some implications for fatigue cracks in a typical offshore mooring chain link are furthermore addressed.

2. Methods

2.1. Geometry and crack growth model

A semi-elliptical crack in a curved round bar with diameter D is considered (Fig. 2). The elliptical crack front is defined in the x-y plane, with semi-axes a_{elp} and b_{elp}. For an almond shaped crack (Fig. 2a), the ellipse origin is at the coordinate system origin, and the crack depth is $a = a_{elp}$. For a sickle shaped crack (Fig. 2b), the ellipse origin is moved to the opposite side of the bar, and the crack depth is $a = D - a_{elp}$. The bar (Fig. 2c) has a radius of curvature R_c in the y-z plane, with center of curvature located on either the cracked- or uncracked side of the bar. For SIF calculation purposes, this geometry and locations along the crack front will be characterized by four dimensionless parameters α, β, γ and ξ defined as follows:

- The crack shape parameter α is defined so that $\alpha > 0$ for almond shaped cracks, $\alpha < 0$ for sickle shaped cracks, and $\alpha = 0$ in the case of

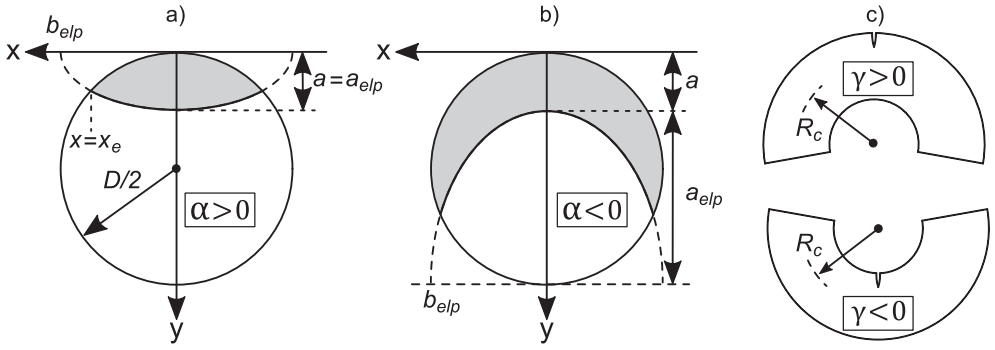

Fig. 2. Parametric description of a curved bar with crack. Definitions are shown for (a) almond shaped crack, (b) sickle shaped crack, and (c) bar curvature. Shaded areas represent the crack. Sign conventions for α and γ have been included.

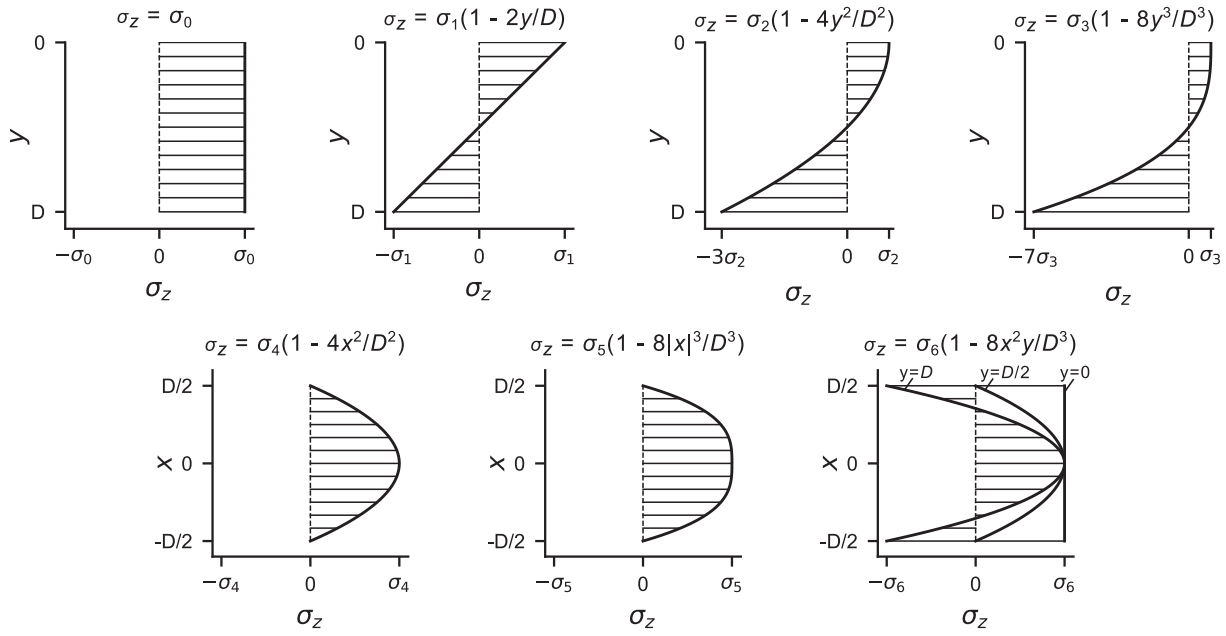

Fig. 3. Elementary mode I stress distributions.

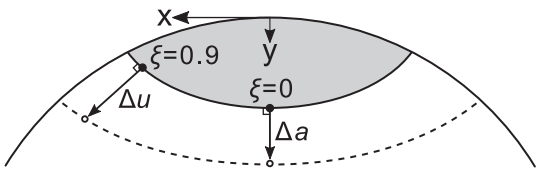

Fig. 4. Incremental crack shape updating method for fatigue crack growth simulations.

a straight-fronted crack. Its absolute value $|\alpha|$ is in any case equal to the ellipse aspect ratio a_{elp}/b_{elp}.

- The relative crack depth is $\beta = a/D$.
- The relative bar curvature γ is defined so that $\gamma > 0$ if the crack is on the outer radius of the bar, $\gamma < 0$ if the crack is on the inner radius of the bar, and $\gamma = 0$ for a straight bar. Its absolute value $|\gamma|$ is in any case D/R_c.
- The exact location of a point on the crack front is specified as $\xi = |x/x_e|$, where x_e is the x-coordinate for the intersection point between the crack front and the bar surface.

The crack is subjected to Mode I loading where the normal stress distribution σ_z in the crack plane, before any crack has been introduced, can be defined by the following polynomial function:

$$\sigma_z(x,y) = \sigma_0 + \sigma_1(1-2y/D) + \sigma_2\left(1-4y^2/D^2\right) + \sigma_3\left(1-8y^3/D^3\right) + \sigma_4\left(1 - 4x^2/D^2\right) + \sigma_5\left(1-8|x|^3/D^3\right) + \sigma_6\left(1-8x^2y/D^3\right) \quad (1)$$

This stress distribution can in the case of a straight bar under tension loading be reduced to a uniform tensile stress $\sigma_z = \sigma_0$, or for a straight bar under bending load reduced to a linear bending stress $\sigma_z = \sigma_1(1-2y/D)$. In general, it represents a superposition of seven elementary mode I stress distributions (Fig. 3). For more complex loading conditions and/or residual stress fields, the stress distribution in the crack plane can be approximated by determining best-fit values for the reference stresses $\sigma_i = \sigma_0, \ldots, \sigma_6$ in Eq. (1). The quadratic and cubic terms in x have been included to allow for a more accurate approximation of some stress distributions that can be relevant for mooring chain links. See for example the residual stress distributions indicated by Bastid and Smith [4], as well as the stress analysis results presented in Section 3.3 of the present paper. Note however that since Eq. (1) does not contain any terms that are linear in x, it can only represent stress distributions that are smooth and symmetric over the $x = 0$ plane.

Fatigue crack growth is in this work modelled using an incremental crack shape updating method based on a model presented by Carpinteri [9], Couroneau and Royer [10]. The method is illustrated in Fig. 4. It is assumed that that the local crack growth rate in a direction perpendicular to any point on the crack front is described by a crack growth law in the form $da/dN = f(\Delta K_{eff})$. The effective stress intensity factor at the same point is $\Delta K_{eff} = U^* \Delta K$, where $\Delta K = \Delta K_I(\ldots,\xi)$ is the local SIF range and U is the effective stress intensity factor ratio. The latter parameter may be used for representing e.g. crack closure and/or stress ratio effects. For the sake of simplicity, two points on the crack front can be considered, located at the center of the crack ($\xi = 0$) and near the crack front edge ($\xi = 0.9$). If the crack depth a is incremented by a small distance Δa, it follows that the local crack increment distance Δu at the crack front edge position can be approximated as:

$$\Delta u = \Delta a \frac{da/dN(\xi = 0.9)}{da/dN(\xi = 0)} \quad (2)$$

Using this method, a numerical crack growth calculation can be performed by incrementally propagating the crack front in small steps of Δa while updating the crack shape parameter α. At the start of each crack growth increment, the semi-elliptical crack front is represented by a set of discrete points. While fatigue crack growth calculations in the present work have been performed using two points, any number of points can be used as long as it is no less than two. For each individual point, Δu is determined, and its corresponding coordinates on the updated crack front calculated by extending a vector of length Δu in a direction perpendicular to the initial crack front. In the special case of a point located at the center of the crack front ($\xi = 0$), Δu is equal to Δa. At the end of the increment, the shape parameter α of the updated crack front is determined by fitting an ellipse to the new coordinates. If the crack front is represented by more than two points, a least squares ellipse fitting procedure can be used for this purpose. The number of accumulated fatigue cycles N can finally be determined by integration of the fatigue crack growth law.

From Eq. (2) it can be seen that the crack shape development predicted by this model depends on the crack growth law as well as the

Table 1
Parameters for FEA model. The lower limit for α is -1.2 for $\beta > 0.40$, and -1.5 otherwise.

	Symbol	Lower limit	Upper limit
Crack shape parameter	α	-1.5 (-1.2)	1.5
Relative crack depth	β	0.03	0.50
Bar curvature parameter	γ	-1.2	1.2
Relative crack front position	ξ	0.00	0.82

variation in ΔK_{eff} over the crack front. A SIF solution suitable for calculating local ΔK on all intermediate crack front shapes encountered during the crack growth calculation is accordingly needed.

2.2. SIF calculations

Mode I stress intensity factors (SIFs) are in this work evaluated for a variety of almond- and sickle shaped semi-elliptical cracks in curved round bars. As is detailed in Section 2.1, crack geometry is defined by parameters α and β, bar curvature is defined by γ, while the stress distribution is defined by Eq. (1). Using the principle of superposition, the local SIF at crack front position ξ can then be expressed as:

$$K_I = \sum_{i=0}^{6} F_i(\alpha, \beta, \gamma, \xi)\sigma_i\sqrt{\pi a} \tag{3}$$

The functions $F_i(\alpha,\beta,\gamma,\xi)$ are dimensionless geometry correction factors associated with the corresponding reference stresses σ_i in the stress distribution. Semi-analytical approximate solutions are in the present work developed for these functions using sets of finite element analysis (FEA) results.

Geometry correction factors F_i for each component of the stress distribution are first numerically calculated using FEA of semi-elliptical crack models. Parameter ranges for the FEA models are summarized in Table 1. These geometries include 15 different crack shape parameters α, 9 different crack depths β, and 7 different bar curvatures γ. In the special case of $\beta > 0.40$, the most extreme of the sickle-shaped crack geometries ($\alpha = -1.5$) are excluded. The length of the bar is equal to $3D$ for all geometries. In total, 938 different geometries are considered for each of the 7 elementary stress distributions. Each geometry is meshed using 20-node hexahedral elements, using collapsed-node elements with mid-side nodes moved to quarter-point positions around the crack front (Fig. 5). Since the model has two symmetry planes, only a quarter of the bar is included in the FEA mesh. Material properties are modelled as isotropic and linear elastic with Poisson's ratio $\nu = 0.3$. Loading is

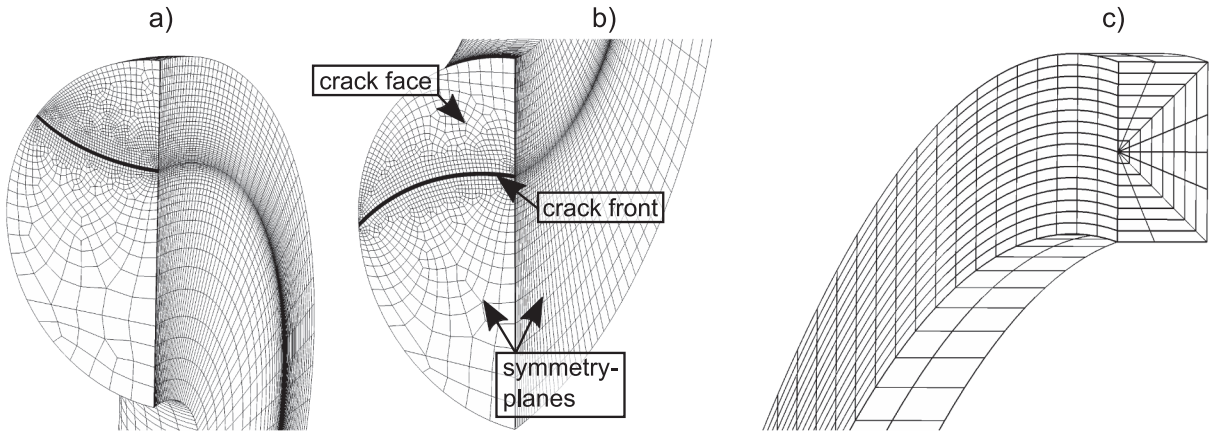

Fig. 5. FEA mesh examples. Images show quarter-bar models for (a) almond shaped crack with bar curvature $\gamma > 0$, (b) sickle shaped crack with bar curvature $\gamma < 0$, and (c) detail of crack front mesh.

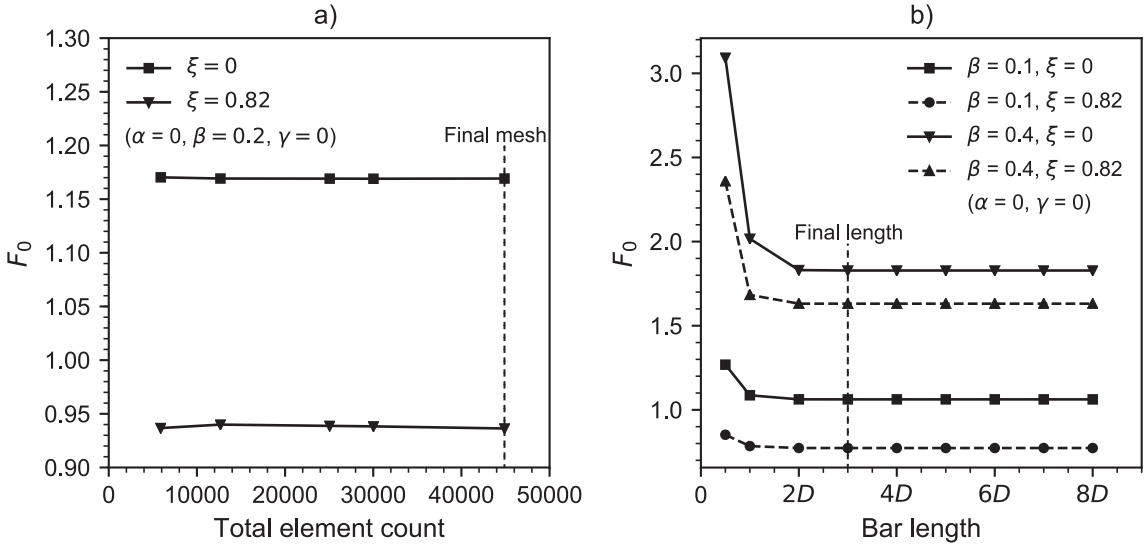

Fig. 6. FEA results in the form of calculated geometry correction factors for selected crack geometries under tension loading, showing (a) mesh refinement study and (b) an investigation into the effect of bar length.

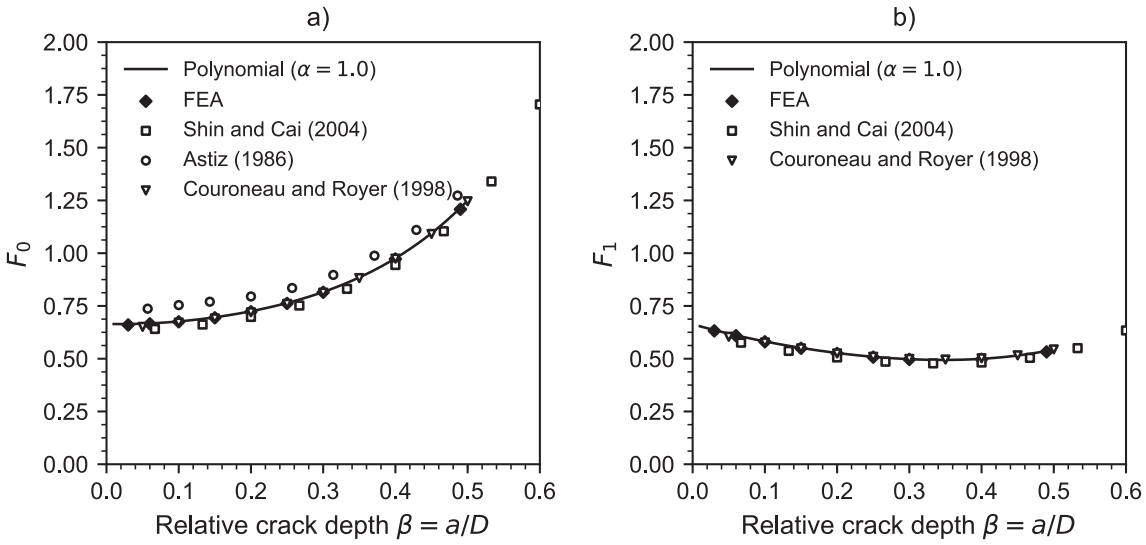

Fig. 7. Geometry correction factors at center of almond shaped semi-circular crack front in straight bar, for (a) tension and (b) bending load.

accomplished by applying a crack-face pressure boundary condition corresponding to the desired stress distribution. For each crack geometry, F_i values are extracted from 10 equally spaced points on the crack front. Analyses were performed using the commercial software Abaqus 2017, with conversion from J-integral values to geometry correction factors F_i performed under the assumption of plane strain conditions. An overview of all FEA results is provided in the accompanying dataset [18]. Semi-analytical solutions for $F_i(\alpha,\beta,\gamma,\xi)$ are finally developed by least-squares fitting of polynomial expressions to the FEA results.

The finite element meshing strategy and choice of bar length used in the present FEA models can be supported by the data presented in Fig. 6. Results from a mesh refinement study performed on one of the crack geometries are presented in Fig. 6a. The final meshing strategy can be seen to use significantly smaller element sizes than what appears to be required for convergence. This additional refinement is in part intended to aid the meshing software in readily producing acceptable meshes for the full range of different crack geometries. Results from an investigation into the effect of bar length on FEA results are furthermore presented Fig. 6b. While the magnitude of this effect is considerable for relatively short bars, it appears to diminish rapidly when extending the bar length beyond approximately $2D$. It can also be noted that since the final bar length is equal to $3D$, none of the bar curvature parameters considered in this work result in self-intersecting model geometries.

For a surface breaking crack in a round bar, it is well known that the linear elastic stress singularity associated with the crack front can deviate from the classical square root relationship when approaching the free surface [19–21]. This implies that the conventional SIF definition may be considered unsuitable inside a near-surface boundary layer. In order to lessen the effect of the near-surface boundary layer on the semi-analytical solutions, FEA results from crack front positions characterized by $\xi > 0.82$ are therefore disregarded. The choice of $\xi = 0.82$ as a cutoff point was the result of a pragmatic trial and error process aimed at ensuring that the variation in FEA results over any of the considered crack fronts could be reasonably approximated using cubic polynomial functions. It can be noted that this cutoff position is comparable to what has been used in some earlier studies by Shin and Cai [12] as well as Rubio et al. [16], in which FEA results from crack front positions up to $\xi \approx 0.83$ were used when developing polynomial solutions. For positions characterized by $\xi > 0.82$, the polynomial expressions presented in this work will accordingly yield extrapolated values.

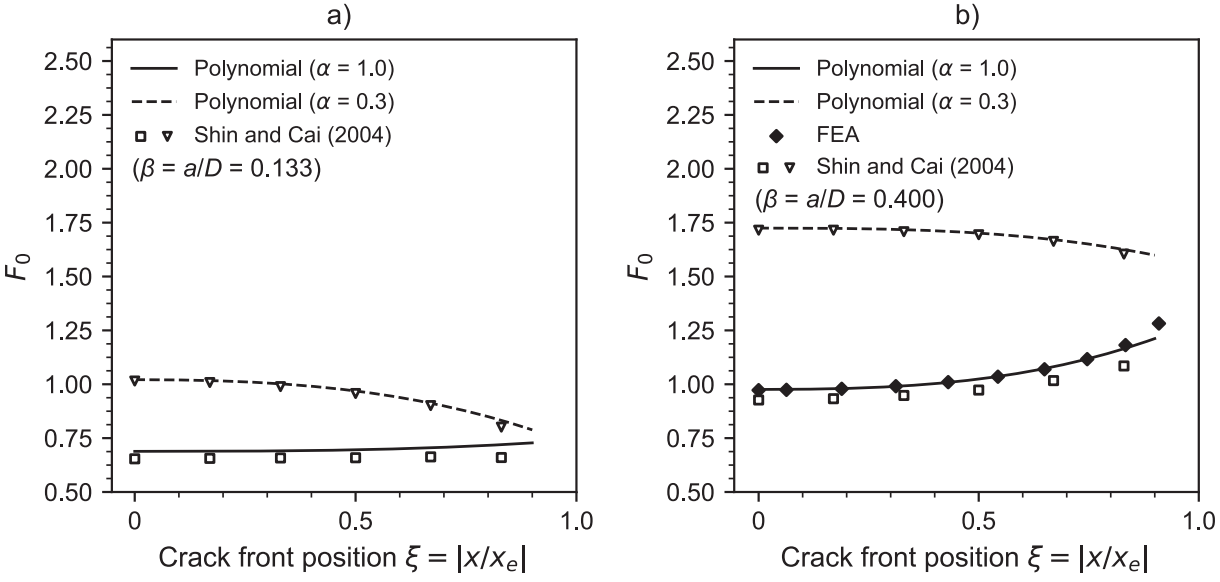

Fig. 8. Geometry correction factor variation over almond shaped crack fronts in tension loaded straight bar.

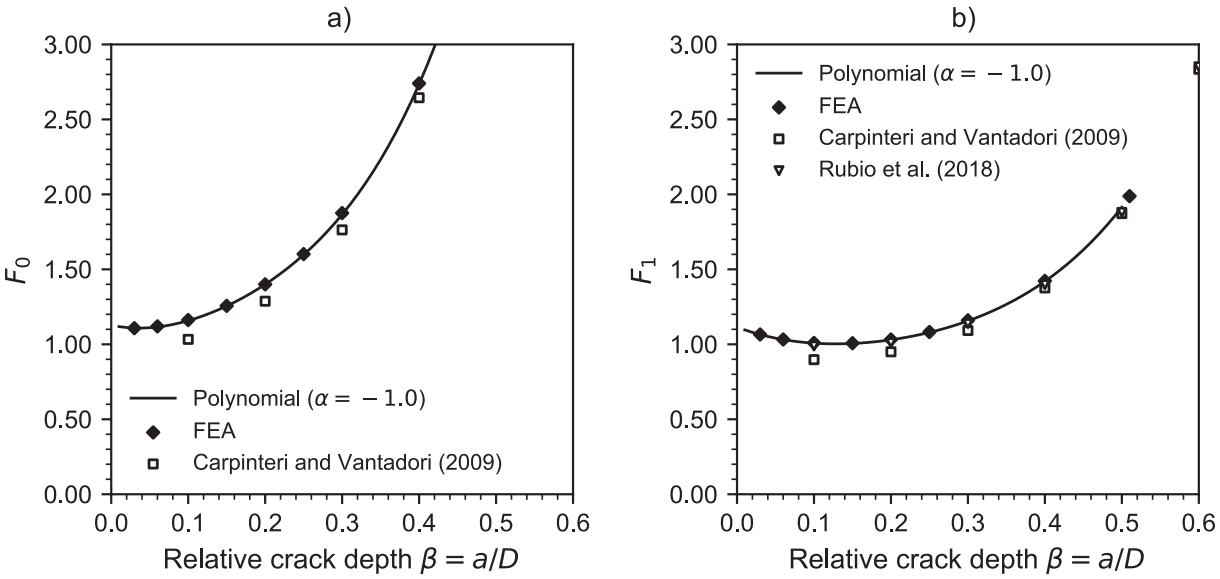

Fig. 9. Geometry correction factors at center of a sickle shaped semi-circular crack front in a straight bar, for (a) tension and (b) bending load.

The total number of discrete $F_i(\alpha,\beta,\gamma,\xi)$ values from FEA used in fitting each semi-analytical polynomial function F_i is 8120. Since a variety of higher-order polynomials were considered for these functions, the final polynomial expressions were chosen by weighing the sizes of the candidate polynomials against prediction errors estimated using leave-one-out and k-fold cross validation techniques.

3. Results and discussion

3.1. SIF solution

The semi-analytical solutions for the dimensionless geometry correction factors F_i were chosen to be polynomial expressions of the following form:

$$F_i(\alpha,\beta,\gamma,\xi) = \sum_{q=0}^{9}\sum_{r=0}^{4}\sum_{s=0}^{2}\sum_{\substack{t=0\\ t\neq 1}}^{3} C_{i,qrst}\alpha^q\beta^r\gamma^s\xi^t \tag{4}$$

Each individual function $F_i = F_0,\ldots,F_6$ corresponds to the stress component with reference stress σ_i in the stress distribution, i.e. Eq. (1), and contains 450 non-zero coefficients $C_{i,qrst}$. Any 0^0 terms in the expressions must be evaluated to 1. When only evaluating at the two points $\xi = 0.0$ and $\xi = 0.9$, the following simplified expressions can be used:

$$F_i(\alpha,\beta,\gamma,\xi = 0.0) = \sum_{q=0}^{9}\sum_{r=0}^{4}\sum_{s=0}^{2} A_{i,qrs}\alpha^q\beta^r\gamma^s \tag{5}$$

$$F_i(\alpha,\beta,\gamma,\xi = 0.9) = \sum_{q=0}^{9}\sum_{r=0}^{4}\sum_{s=0}^{2} B_{i,qrs}\alpha^q\beta^r\gamma^s \tag{6}$$

Best-fit coefficients $A_{i,qrs}$, $B_{i,qrs}$ and $C_{i,qrst}$ are provided in an accompanying dataset [18]. See also Appendix A. The polynomial fits all have a coefficient of determination R^2 of 0.9999 or higher, while their relative errors compared to the FEA results are no higher than 3.2%.

In the special case of a straight bar under tension- or bending load, the polynomial stress intensity factor (SIF) solution defined by Eq. (3) and Eq. (4) can readily be compared to results published by other

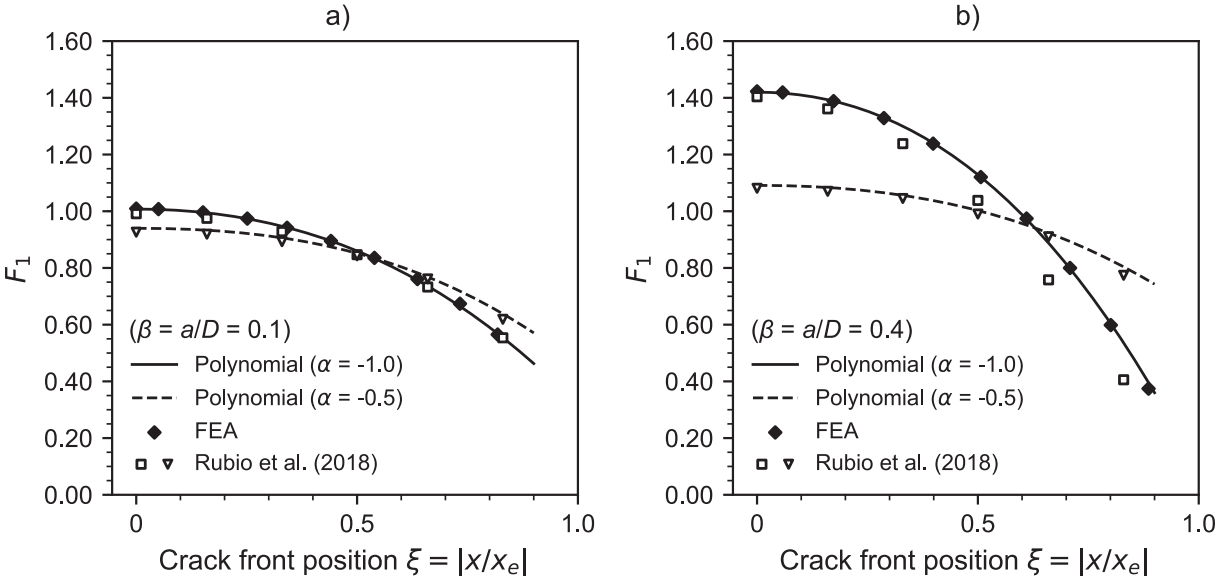

Fig. 10. Geometry correction factor variation over sickle shaped crack fronts in straight bars under bending load.

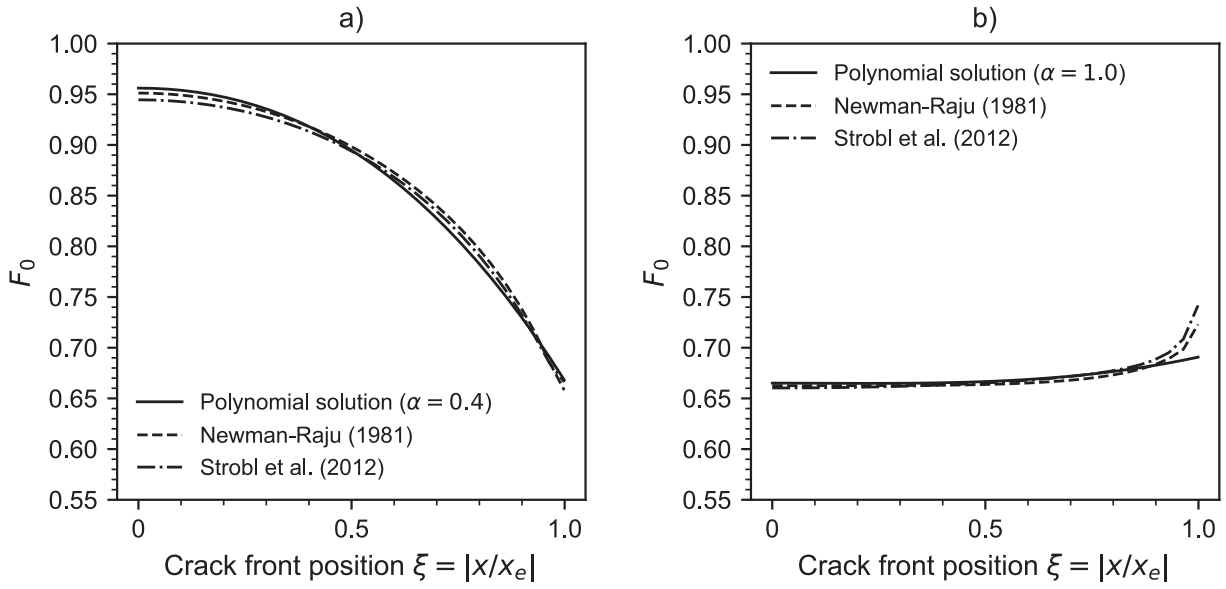

Fig. 11. Variation in geometry correction factor over the crack front when relative crack depth approaches zero. Showing (a, b) two different crack shapes α.

authors. Fig. 7 shows geometry correction factors at the $\xi = 0$ crack front center position on an almond shaped semi-circular crack. Comparisons are made against FEA results reported by Astiz [8], Couroneau and Royer [10], as well as Shin and Cai [12]. FEA results from the present work are also included. The variation in F_0 over the crack fronts of selected almond shaped cracks is furthermore shown in Fig. 8. Note that, since the discrete crack geometries considered in FEA differ among the different studies, FEA results from the present work are not available for all selected cracks. Also note that the FEA results from $\xi > 0.82$ were disregarded when fitting the polynomial solutions. Some smaller deviations from the results reported by Shin and Cai can be found when approaching the bar surface at $\xi = 1.0$. The single largest difference corresponds to a 9% increase in F_0 compared to the literature data. Overall, the present SIF solution does however agree reasonably with the literature data.

For sickle shaped cracks of various shapes, Fig. 9 shows geometry correction factors F_0 and F_1 at the $\xi = 0$ crack front position, while Fig. 10 shows variation in F_1 over the crack fronts. Comparisons have been made against FEA results from Carpinteri and Vantadori [15], as well as Rubio et al. [16]. Deviations from the results reported by Rubio et al. can be seen for the large semi-circular sickle shaped crack ($\alpha = -1.0$, $\beta = 0.4$), where the present polynomial solution appears to yield noticeably higher values. Reasonable agreement between the present SIF solution and literature data does however appear to exist for the remaining geometries.

Another special case that can be useful for verification purposes is that of a semi-elliptical crack in a round bar when the relative crack depth β approaches zero. A given almond shaped surface crack ($\alpha > 0$) in a round bar can in this case be considered to have nearly identical geometry to that of the same crack located in a semi-infinite plate. The variation in F_0 over the crack fronts of selected cracks characterized by $\beta \approx 0$ is shown in Fig. 11. Comparisons are made against the closed form solution for surface cracks in plates published by Newman and Raju [22], as well as the more recent solution by Strobl et al. [23]. An assumption of $\nu = 0.3$ is made when implementing the latter solution. Some disagreement between the solutions can be identified in the near-

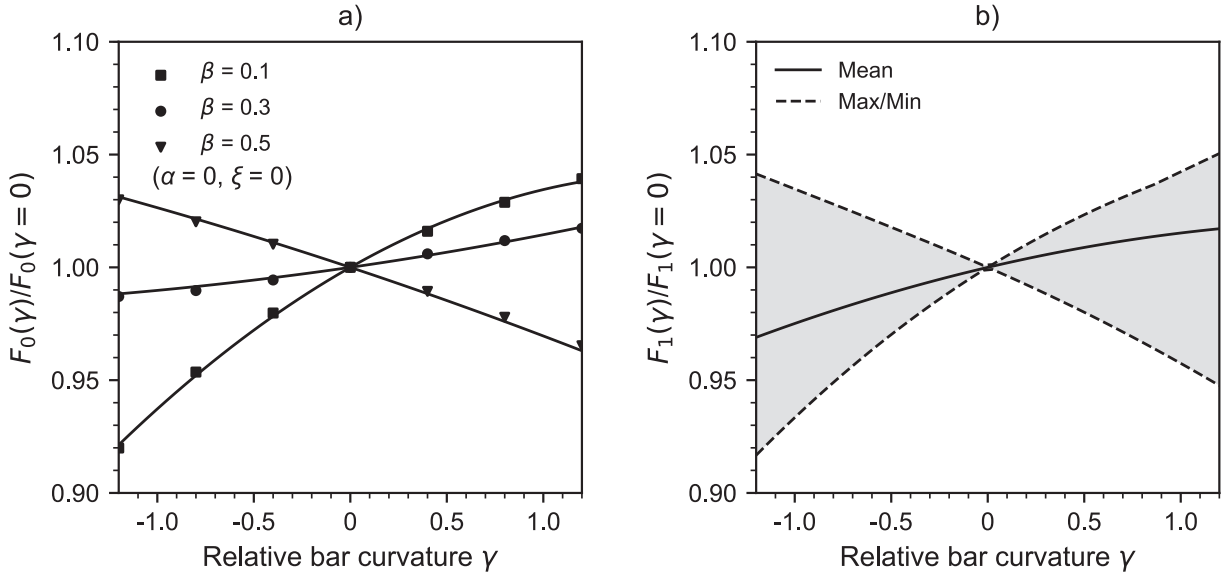

Fig. 12. Effect of bar curvature on SIF at (a) center of selected straight-fronted cracks under uniform tensile stress and (b) mean effect over the full range of considered geometries and crack front positions under linear bending stress.

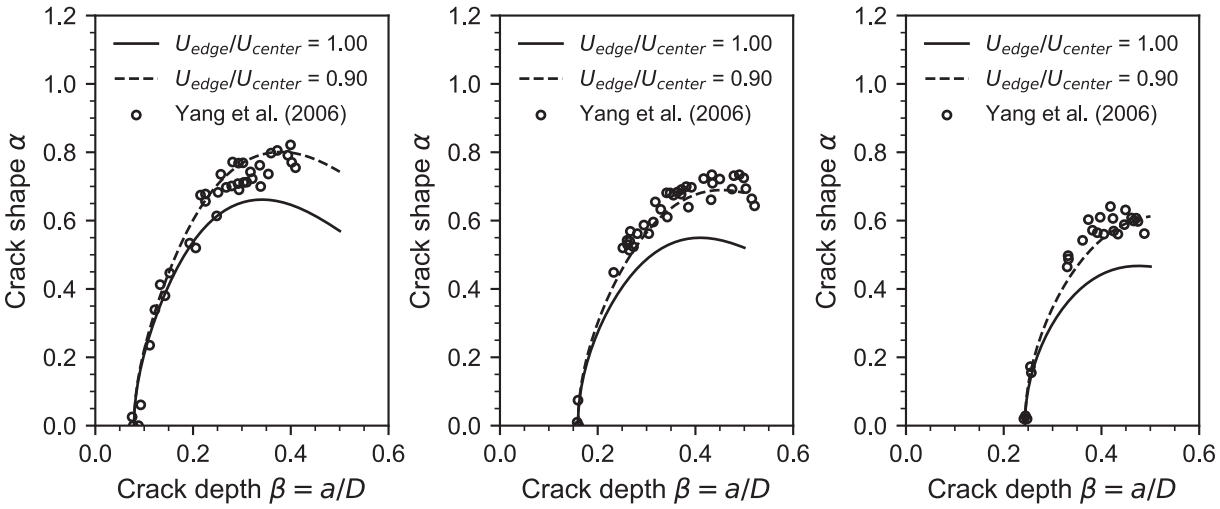

Fig. 13. Crack shape development calculated for initially flat-fronted fatigue cracks under cyclic tension loading, showing results for three different initial crack depths.

surface boundary layer. Since the present polynomial solution uses extrapolation in this region ($\xi > 0.82$), this is however as expected. The present SIF solution can otherwise be seen to be consistent with the literature solutions for this semi-infinite geometry.

The curvature of the round bar component is found to have a discernable effect on calculated SIFs. Fig. 12 shows the effect of bar curvature on SIFs associated with different straight-fronted cracks. Values shown in Fig. 12a are geometry correction factors F_0 for the $\xi = 0$ crack front position, normalized by the corresponding values for the same crack in a straight bar ($\gamma = 0$). The polynomial SIF solution is shown as full lines while FEA results are indicated by markers. A non-trivial relationship between bar curvature and SIF can be observed. For smaller relative crack depths $\beta = a/D$, the SIFs tend to increase with increasing curvature parameter γ. As the crack becomes deeper however, an opposite trend appears.

Fig. 12b shows a mean effect plot obtained by considering all geometries and crack front positions within the parameter limits defined in Table 1, including min/max bounds. Although this diagram only shows results for bending stress, the magnitude of the bar curvature effect was found to be approximately the same for all seven elementary stress distributions. Across all stress distributions and geometries considered, the single largest error that can be introduced by disregarding bar curvature effects is found when the relative bar curvature corresponds to $\gamma = -1.2$. The calculated SIF at the center of a flat-fronted crack ($\alpha = 0$, $\xi = 0$) with relative depth $\beta = 0.1$ is in this case 8% lower than for the same crack in a straight bar.

3.2. Fatigue crack growth in a straight bar

For validation of the semi-analytical SIF solutions when used with the numerical fatigue crack growth model from Section 2.1, predicted crack shape development is compared against a set of experimental measurements. A straight bar of diameter $D = 12$ mm containing various flat-fronted cracks is considered. Initial crack depths a are 1, 2 and 3 mm. Comparisons are made against crack shape measurements adapted from Yang et al. [24], where fatigue loading of steel bars with this geometry had been performed at a stress ratio of $\sigma_{min}/\sigma_{max} = 0.1$.

Numerical calculations have been performed with the crack front represented by two nodes located at the crack front center ($\xi = 0$) and near the crack front edge ($\xi = 0.9$), respectively. Crack depth incrementation has been performed in steps of $\Delta a = D/2000$ while assuming a Paris-Erdogan crack growth law on the form $da/dN = 1e^{-8}(\Delta K_{eff})^3$ mm/cycle. Since it has been shown by several authors [25–27] that plasticity induced crack closure tends to become more pronounced near free surfaces, a possible variation in the effective stress intensity factor ratio $U = \Delta K_{eff}/\Delta K$ over the crack front is considered. If $U = U_{center}$ at the center of the crack and $U = U_{edge}$ at the free surface, the effect on crack shape development is determined by the crack closure factor ratio U_{edge}/U_{center}. A ratio of $U_{edge}/U_{center} = 1.0$ implies that crack closure has no effect on crack shape development. Newman and Raju [28] suggested to use $U_{edge}/U_{center} = 0.9 + 0.2*(\sigma_{min}/\sigma_{max})^2 + 0.1*(\sigma_{min}/\sigma_{max})^4$ for positive stress ratios, which in the case of $\sigma_{min}/\sigma_{max} = 0.1$ evaluates to a ratio of about 0.902. Measurements performed by Song and Shieh [29] on a surface crack in steel under constant amplitude fatigue loading at a stress ratio of $\sigma_{min}/\sigma_{max} = 0.1$ similarly suggested an average U_{edge}/U_{center} ratio of approximately 0.92. Crack growth calculations are therefore performed assuming U_{edge}/U_{center} ratios of 1.0 and 0.9, with U_{center} applied to the crack front node at $\xi = 0$ and U_{edge} applied to the node at $\xi = 0.9$.

Results from the numerical crack growth calculations are shown in Fig. 13. When crack closure effects are disregarded ($U_{edge}/U_{center} = 1.0$), the cracks are predicted to develop a somewhat more flat-fronted shape than experimentally observed. This suggests some overestimation of the effective crack driving force near free surfaces relative to the interior regions of the crack. Good agreement with the experimental data is however achieved when correcting for plasticity induced crack closure effects by assuming $U_{edge}/U_{center} = 0.9$.

3.3. Implications for cracks in offshore mooring chain links

In order to comment on the practical usefulness of the present model, an offshore mooring chain link with bar diameter $D = 114$ mm is considered as a practical case example. A comparison has been performed between the full model and a simplified case, in which bar curvature is disregarded and the stress distribution is approximated as a linear combination of tension and bending stress. A semi-circular crack ($\alpha = 1.0$) is located at the crown of the chain link, i.e. in the plane labelled as location 1 in Fig. 1. Relative bar curvature in this region corresponds to $\gamma = 0.85$. The chain link is assumed to have been subjected to an initial proof loading during manufacture, before any crack has been introduced. As is specified by DNVGL-OS-E302 [30] for a grade R4 chain of this geometry, the proof loading is performed by applying a tensile load $P = P_{proof} = 8703$ kN to the chain, corresponding to 70% of its minimum specified breaking load. This process results in localized plastic deformation, and after unloading, introduces compressive residual stresses in the crack location of interest.

The proof loaded chain is then assumed to experience a cyclic fatigue load ranging between $P_{max} = 3105$ kN and $P_{min} = 1863$ kN,

Table 2
Best-fit stress distributions representing normal stresses to crack plane in chain link with residual stresses.

Stress distribution	Load level	σ_0 [MPa]	σ_1 [MPa]	σ_2 [MPa]	σ_3 [MPa]	σ_4 [MPa]	σ_5 [MPa]	σ_6 [MPa]
Linear	P_{max}	386.2	−350.5	0	0	0	0	0
	P_{min}	316.7	−511.3	0	0	0	0	0
7-term	P_{max}	655.0	−120.0	54.1	−193.6	69.3	−113.2	−256.1
	P_{min}	570.9	−273.9	63.5	−218.9	102.2	−97.7	−273.0

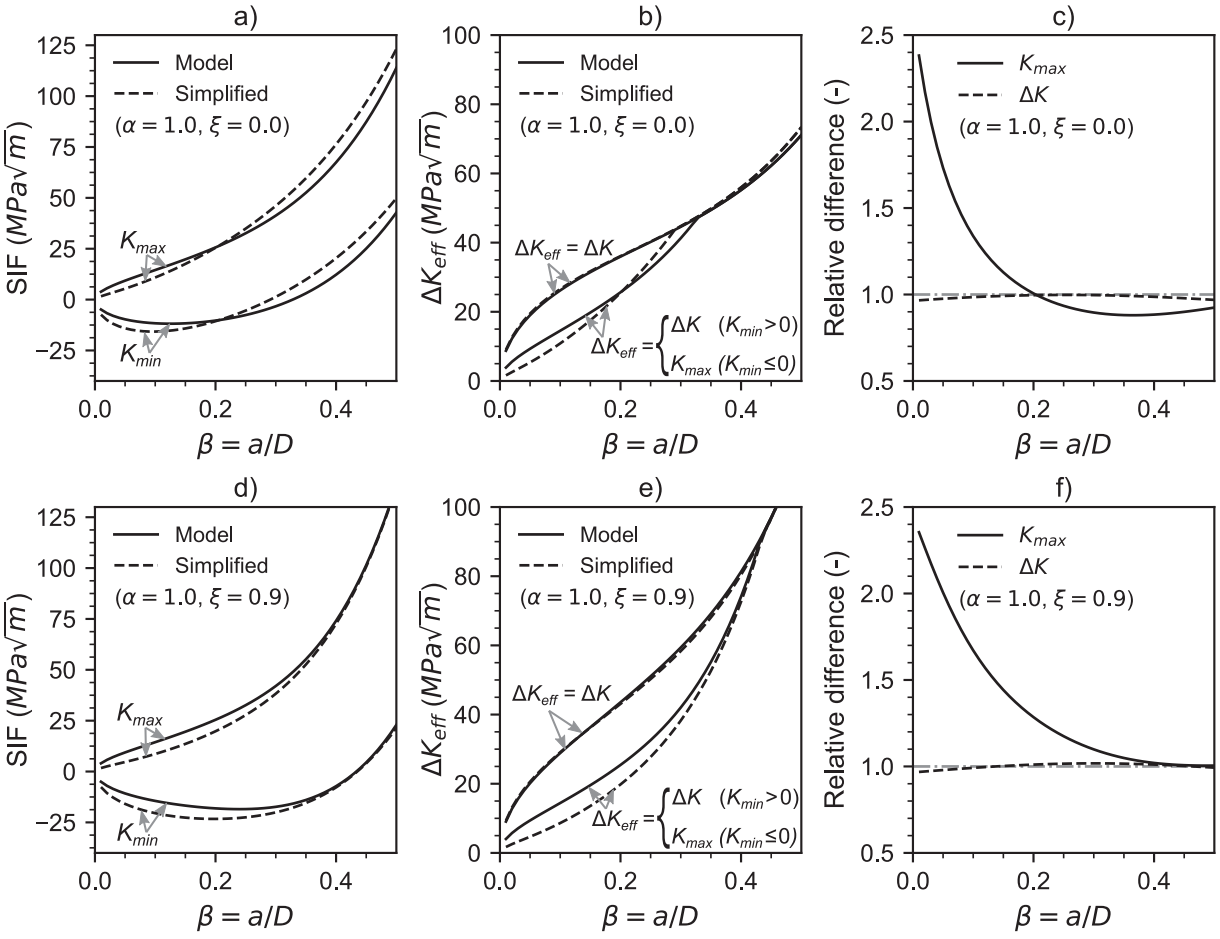

Fig. 14. Effects of bar curvature and choice of polynomial stress definition on SIFs for an example crack in the chain link model. The full model is compared with a simplified case that assumes straight bar and linearized stress field. Results are shown for (a-c) the $\xi = 0$ crack front position and for (d-f) the $\xi = 0.9$ position.

corresponding to 25% and 15% of its minimum breaking load. A stress analysis of the uncracked chain link geometry subjected to these loading conditions is performed using elastic–plastic finite element analysis (FEA). Boundary conditions and material model are taken as identical to that used by Zarandi and Skallerud [31]. Least-squares fitting to FEA results is then used to approximate the resulting stress distributions in the crack plane between the crack origin ($y = 0$) and half-thickness position ($y = D/2$) as polynomial functions. Two stress approximations have been considered; a simplified linear stress distribution and the more comprehensive 7-term polynomial represented by Eq. (1). Values for the resulting best-fit stress distributions used in this example are provided in Table 2. Due to the residual stresses, the situation near the crack origin can be characterized as being in compression at P_{min} and transitioning to tension at P_{max}.

Stress intensity factors K_{min} and K_{max} calculated for the two load levels P_{min} and P_{max} are shown in Fig. 14. The curves labelled "Model" represent results calculated when taking bar curvature into account and using the 7-term polynomial stress approximation. The curves labelled "Simplified" represent results calculated when assuming that the bar is straight, and the linear stress approximation is used. Resulting effective stress intensity factor ranges ΔK_{eff} are also included, as well as plots highlighting relative differences. Subplots a-c show results from the center of the crack ($\xi = 0$) while d-f show results from the near-edge position ($\xi = 0.9$). Note that, since stresses near the crack origin are compressive at P_{min}, the resulting K_{min} also assume negative values in this region. Negative SIF values are in general not physically meaningful, implying that ΔK by itself in this case might be inadequate for representing crack driving force. In addition to $\Delta K_{eff} = \Delta K$, curves representing the simple assumption of $\Delta K_{eff} = K_{max}$ whenever $K_{min} <= 0$ has therefore been included as well.

From the results shown in Fig. 14, it is evident that curvature and choice of polynomial stress field representation in this example case end up having no significant effects on calculated ΔK. Considering K_{max} on the other hand, which is influenced by residual stresses, the 7-term polynomial stress approximation can be seen to potentially provide a far more accurate SIF representation than the linearized stress representation. At a relative crack depth $\beta = 0.1$, the differences in calculated ΔK values are less than 2%, while K_{max} values differ by about 34% at the

Table A1
Polynomial coefficients for pure tensile stress.

		$A_{0,qrs}$ ($\xi = 0$)			$B_{0,qrs}$ ($\xi = 0.9$)		
q	r	$s = 0$	$s = 1$	$s = 2$	$s = 0$	$s = 1$	$s = 2$
0	0	1.0986	0.0085	−0.0105	0.5841	−0.0043	−0.0011
0	1	−1.3039	0.8380	−0.1986	0.9256	0.2647	−0.0476
0	2	11.1412	−5.0147	2.0243	3.6551	−1.9986	0.5865
0	3	−20.0905	10.2996	−5.2847	−7.9855	3.8137	−1.6279
0	4	29.5980	−8.5500	4.1484	21.6522	−2.8994	1.0539
1	0	−0.1344	−0.0112	0.0053	0.3315	0.0014	−0.0162
1	1	0.9933	0.1036	−0.0887	−4.4648	0.4510	0.1208
1	2	−5.6901	−0.2993	0.4658	23.5223	−3.4859	−0.2074
1	3	13.0322	0.5697	−1.1220	−51.9053	8.9003	−0.1619
1	4	−13.5603	−0.3873	1.0891	40.1995	−7.6296	0.4136
2	0	−0.4859	−0.0229	0.0202	0.3799	0.0171	0.0071
2	1	1.9626	−0.2629	−0.1516	−2.0933	0.6957	−0.7118
2	2	−4.4536	3.3055	−0.1853	−1.7497	−2.1921	5.3879
2	3	−6.5530	−8.5433	2.3889	30.1609	−2.3817	−13.6096
2	4	23.3589	6.3626	−3.1872	−40.1889	7.6412	11.1595
3	0	−0.4468	0.0225	0.0060	−0.8627	0.0170	0.0722
3	1	0.9717	−1.4363	0.2307	17.1280	−0.6983	−1.5070
3	2	−17.7617	9.9631	−2.5129	−106.3898	12.4853	6.5683
3	3	52.2199	−22.2907	6.7266	249.9532	−40.1780	−7.5695
3	4	−77.9473	18.9124	−4.9500	−194.9282	33.6757	0.6660
4	0	0.4857	0.0387	−0.0288	−0.6516	−0.0220	−0.0241
4	1	−2.2050	−0.1614	0.3623	0.8537	−1.6472	1.6577
4	2	2.0054	−1.7473	−0.5768	21.3136	7.1079	−13.1726
4	3	21.0262	5.4897	−2.2345	−111.0221	−0.3989	33.9083
4	4	−36.9194	−3.0985	4.1940	113.9855	−11.0925	−27.1931
5	0	0.6377	−0.0353	−0.0133	1.0647	−0.0585	−0.0928
5	1	−3.3013	1.8868	−0.0526	−23.7312	1.0213	2.1914
5	2	33.9234	−14.1639	1.3228	152.0523	−16.8681	−9.7791
5	3	−102.1877	34.5597	−3.4321	−375.1932	55.7707	10.6072
5	4	121.0991	−30.1393	1.7351	315.8876	−48.9200	0.2297
6	0	−0.2463	−0.0248	0.0161	0.3458	0.0124	0.0204
6	1	1.0595	0.2498	−0.2151	1.4294	1.0835	−1.1745
6	2	2.7906	−0.1520	0.3469	−28.1455	−4.9691	9.3112
6	3	−23.6541	−0.4644	1.4646	112.9459	1.3377	−24.1249
6	4	32.2297	−0.2567	−2.8113	−113.3222	6.3405	19.4930
7	0	−0.3616	0.0237	0.0090	−0.5431	0.0484	0.0475
7	1	2.4715	−1.0475	−0.0782	12.6530	−0.6915	−1.1933
7	2	−23.8749	8.2532	0.1826	−82.1191	9.4749	5.3901
7	3	72.6943	−21.2215	−0.6401	208.9585	−31.4449	−5.5097
7	4	−79.3487	18.7429	1.2966	−185.5462	28.7287	−0.8096
8	0	0.0451	0.0051	−0.0030	−0.0492	−0.0026	−0.0049
8	1	−0.1164	−0.0690	0.0394	−0.7192	−0.2221	0.2584
8	2	−1.5954	0.1768	−0.0427	8.8493	1.0470	−2.0392
8	3	7.9354	−0.1930	−0.4023	−32.1348	−0.3659	5.3195
8	4	−9.8045	0.1749	0.7187	32.2526	−1.2667	−4.3512
9	0	0.0713	−0.0051	−0.0020	0.0891	−0.0115	−0.0085
9	1	−0.5955	0.2053	0.0305	−2.2215	0.1527	0.2217
9	2	5.6396	−1.6540	−0.1689	14.5486	−1.8416	−1.0074
9	3	−17.3276	4.3424	0.5134	−37.6583	6.1042	0.9608
9	4	18.4080	−3.8203	−0.6229	34.5431	−5.7235	0.2898

center of the crack (Fig. 14c) and by about 67% at the near-edge position (Fig. 14f). Thus, if the simple assumption of $\Delta K_{eff} = \Delta K$ is made, there does not appear to be any practical advantages to using the more comprehensive model. For alternative ΔK_{eff} definitions that consider the SIF magnitude on the other hand, such as the assumption of $\Delta K_{eff} = K_{max}$ whenever $K_{min} <= 0$, the 7-term polynomial stress representation appears to be capable of providing substantially more accurate representations of the ΔK_{eff} variation over the crack front.

4. Conclusion

Mode I stress intensity factors (SIFs) for semi-elliptical cracks in curved round bars have been evaluated using finite element analysis. Closed-form semi-analytical solutions for approximation of the SIF at any point on an almond- or sickle shaped crack front have furthermore been developed for several elementary mode I stress distributions. The given solutions are intended for use in fatigue crack growth analysis problems involving curved bar geometries, such as chain links. Conclusions that have been drawn from the present work are as follows:

- Numerical crack growth calculations based on the closed-form SIF solutions predict crack shape development curves that compare reasonably well with empirical observations for cracks in straight bars. Some overestimation of the effective crack driving force near free surfaces does however become apparent when crack closure effects are disregarded.
- Bar curvature by itself has a comparably minor effect on SIFs. Relative to an otherwise identical crack in a straight bar, SIFs for cracks in the curved bar geometries considered by this study are found to differ by up to 8%. The exact relationship between bar curvature and its effect on SIFs appears to be non-trivial and crack geometry dependent.
- In the industrially relevant case of proof loaded chain links, the cubic polynomial stress approximation $\sigma_z = \sigma_z(x, y)$ used in the present SIF solutions is found to be useful when the effect of residual stresses on SIF magnitudes (K_{max}) over the crack front is of interest. While a

Table A2
Polynomial coefficients for linear bending stress.

		$A_{1,qrs}$ ($\xi = 0$)			$B_{1,qrs}$ ($\xi = 0.9$)		
q	r	$s = 0$	$s = 1$	$s = 2$	$s = 0$	$s = 1$	$s = 2$
0	0	1.0942	0.0100	−0.0111	0.5844	−0.0037	−0.0014
0	1	−2.4672	0.7690	−0.1625	0.0331	0.2408	−0.0333
0	2	9.2696	−4.9260	1.8092	0.7963	−2.0375	0.5309
0	3	−15.3633	10.5219	−4.9921	−0.4770	4.4379	−1.6930
0	4	14.9729	−8.2803	4.1889	4.5907	−3.3257	1.4108
1	0	−0.1301	−0.0113	0.0054	0.3079	0.0038	−0.0160
1	1	0.9821	0.1258	−0.0918	−3.1754	0.3858	0.1101
1	2	−4.6054	−0.5175	0.5099	16.2934	−3.0835	−0.1295
1	3	9.1061	1.1853	−1.2509	−36.7282	7.9208	−0.3722
1	4	−7.4704	−1.0536	1.1699	29.6537	−6.7571	0.6336
2	0	−0.4983	−0.0246	0.0208	0.3593	0.0163	0.0049
2	1	2.9255	−0.1821	−0.1994	−0.8304	0.7539	−0.6430
2	2	−10.5623	2.9145	0.3178	−2.0786	−3.3604	4.8549
2	3	16.0166	−8.5707	0.7911	17.3660	2.3106	−12.1100
2	4	−4.9475	7.3835	−1.6349	−24.4346	2.4812	9.8230
3	0	−0.4403	0.0193	0.0056	−0.6782	−0.0024	0.0737
3	1	1.0141	−1.3517	0.2096	13.2673	−0.1751	−1.5392
3	2	−11.9974	9.9368	−2.4015	−73.1376	8.5844	7.4008
3	3	34.4192	−23.7876	7.0705	176.8425	−31.7544	−11.7077
3	4	−42.1543	19.9822	−6.1531	−144.6228	29.3443	5.3935
4	0	0.5076	0.0404	−0.0299	−0.6521	−0.0233	−0.0175
4	1	−3.5704	−0.2400	0.4408	−0.8548	−1.7057	1.4561
4	2	11.6386	−1.3722	−1.4991	18.8696	9.2473	−11.6279
4	3	−12.6744	6.5760	0.8843	−78.0273	−10.1470	29.9859
4	4	−1.3249	−6.2708	1.1864	84.0203	−0.8899	−24.4104
5	0	0.6279	−0.0296	−0.0113	0.7194	−0.0211	−0.0987
5	1	−3.3643	1.7261	−0.0640	−17.7450	0.0506	2.3203
5	2	26.7523	−13.4806	1.4607	104.1412	−9.6149	−11.8143
5	3	−78.4378	34.1949	−4.6293	−261.0106	38.7028	19.6840
5	4	83.9746	−29.4592	3.8944	225.9338	−37.4879	−9.8865
6	0	−0.2634	−0.0252	0.0171	0.3955	0.0147	0.0152
6	1	2.0078	0.2628	−0.2665	1.3001	1.0938	−1.0168
6	2	−4.6572	−0.0426	0.9158	−20.7647	−6.2232	8.0954
6	3	−0.3139	−2.0883	−0.3968	77.1346	7.4877	−20.9990
6	4	8.6903	2.5563	−1.0689	−79.5896	−0.2183	17.2036
7	0	−0.3540	0.0198	0.0072	−0.3318	0.0227	0.0524
7	1	2.4291	−0.9295	−0.0509	9.6176	−0.0364	−1.3020
7	2	−19.0742	7.4526	−0.0255	−57.0251	4.6214	6.8710
7	3	57.4535	−19.5111	0.2748	144.9778	−19.4148	−11.8344
7	4	−59.8067	17.0001	−0.0062	−130.8402	19.5899	6.2100
8	0	0.0496	0.0051	−0.0032	−0.0778	−0.0032	−0.0037
8	1	−0.3502	−0.0630	0.0493	−0.4484	−0.2229	0.2209
8	2	0.2861	0.0820	−0.1459	6.1407	1.3094	−1.7513
8	3	2.2433	0.3158	−0.0748	−21.4680	−1.6711	4.5679
8	4	−4.0256	−0.5351	0.4214	21.7181	0.1502	−3.7772
9	0	0.0691	−0.0042	−0.0016	0.0537	−0.0059	−0.0097
9	1	−0.5593	0.1757	0.0229	−1.7468	0.0122	0.2483
9	2	4.4637	−1.4212	−0.1180	10.2471	−0.8093	−1.3418
9	3	−13.6651	3.7593	0.3282	−26.2273	3.4760	2.3523
9	4	14.1397	−3.2607	−0.3832	24.4172	−3.6097	−1.2525

simpler linear stress approximation can be adequate for approximating the SIF range (ΔK) under nominally elastic cyclic loading, the cubic polynomial approximation is found to provide a far better fit to the calculated residual stress distribution.

CRediT authorship contribution statement

Mads Aursand: Conceptualization, Methodology, Software, Validation, Visualization, Writing - original draft. **Bjørn H. Skallerud:** Supervision, Writing - review & editing.

Declaration of Competing Interest

The authors declare that they have no known competing financial interests or personal relationships that could have appeared to influence the work reported in this paper.

Appendix A

In the case of tension- or bending load, polynomial coefficients $A_{i,qrs}$ and $B_{i,qrs}$ for Eq. (5) and Eq. (6) are provided in Table A1 and Table A2, respectively. The complete set of coefficients, including $C_{i,qrst}$ for Eq. (4), are provided in a separate dataset [18].

References

[1] J. Fernández, W. Storesund, J. Navas, Fatigue performance of grade R4 and R5 mooring chains in seawater, in: ASME 2014 33rd International Conference on Ocean, Offshore and Arctic Engineering, ASME, San Francisco, California, USA, 2014. https://doi.org/10.1115/OMAE2014-23491.
[2] Ø. Gabrielsen, K. Larsen, S.-A. Reinholdtsen, Fatigue testing of used mooring chain, in: ASME 2017 36th International Conference on Ocean, Offshore and Arctic Engineering, Trondheim, Norway, 2017. https://doi.org/10.1115/OMAE2017-61382.
[3] Y.-H. Zhang, P. Smedley, Fatigue performance of high strength and large diameter mooring chain in seawater, in: ASME 2019 38th International Conference on Ocean, Offshore and Arctic Engineering, Glasgow, Scotland, 2019. https://doi.org/10.1115/OMAE2019-95984.

[4] P. Bastid, S.D. Smith, Numerical analysis of contact stresses between mooring chain links and potential consequences for fatigue damage, in: ASME 2013 32nd International Conference on Ocean, Offshore and Arctic Engineering, American Society of Mechanical Engineers, Nantes, France, 2013. https://doi.org/10.1115/OMAE2013-11360.
[5] M. Aursand, B. Skallerud, Numerical simulation of fatigue crack growth in offshore mooring chains, in: MekIT'19 Tenth National Conference on Computational Mechanics, 2019, pp. 61–79.
[6] R.I. Stephens, A. Fatemi, R.R. Stephens, H.O. Fuchs, Metal Fatigue in Engineering, 2 ed., John Wiley & Sons, 2000.
[7] Ø. Gabrielsen, T. Liengen, S. Molid, Microbiologically influenced corrosion on seabed chain in the North Sea, in: ASME 2018 37th International Conference on Ocean, Offshore and Arctic Engineering, American Society of Mechanical Engineers, Madrid, Spain, 2018. https://doi.org/10.1115/OMAE2018-77460.
[8] M.A. Astiz, An incompatible singular elastic element for two- and three-dimensional crack problems, Int. J. Fract. 31 (1986) 105–124, https://doi.org/10.1007/BF00018917.
[9] A. Carpinteri, Shape change of surface cracks in round bars under cyclic axial loading, Int. J. Fatigue 15 (1993) 21–26, https://doi.org/10.1016/0142-1123(93)90072-X.
[10] N. Couroneau, J. Royer, Simplified model for the fatigue growth analysis of surface cracks in round bars under mode I, Int. J. Fatigue 20 (1998) 711–718, https://doi.org/10.1016/S0142-1123(98)00037-1.
[11] Y.-S. Shih, J.-J. Chen, The stress intensity factor study of an elliptical cracked shaft, Nucl. Eng. Des. 214 (2002) 137–145, https://doi.org/10.1016/S0029-5493(02)00022-5.
[12] C.S. Shin, C.Q. Cai, Experimental and finite element analyses on stress intensity factors of an elliptical surface crack in a circular shaft under tension and bending, Int. J. Fract. 129 (2004) 239–264, https://doi.org/10.1023/B:FRAC.0000047784.23236.7d.
[13] J. Toribio, N. Álvarez, B. González, J.C. Matos, A critical review of stress intensity factor solutions for surface cracks in round bars subjected to tension loading, Eng. Fail. Anal. 16 (2009) 794–809, https://doi.org/10.1016/j.engfailanal.2008.06.023.
[14] A. Carpinteri, R. Brighenti, S. Vantadori, D. Viappiani, Sickle-shaped crack in a round bar under complex Mode I loading, Fatigue Fract. Eng. Mater. Struct. 30 (2007) 524–534, https://doi.org/10.1111/j.1460-2695.2006.01125.x.
[15] A. Carpinteri, S. Vantadori, Sickle-shaped cracks in metallic round bars under cyclic eccentric axial loading, Int. J. Fatigue 31 (2009) 759–765, https://doi.org/10.1016/j.ijfatigue.2008.03.006.
[16] P. Rubio, Y. Sanz, L. Rubio, B. Muñoz-Abella, Stress Intensity Factor and propagation of an open sickle shaped crack in a shaft under bending, Theor. Appl. Fract. Mech. 96 (2018) 688–698, https://doi.org/10.1016/j.tafmec.2017.10.008.
[17] P. Rubio, J. Bernal, B. Muñoz-Abella, L. Rubio, A closed expression for the Stress Intensity Factor of concave fatigue cracks in rotating shafts, Eng. Fract. Mech. 214 (2019) 233–247, https://doi.org/10.1016/j.engfracmech.2019.02.034.
[18] M. Aursand, Data for: Mode I stress intensity factors for semi-elliptical fatigue cracks in curved round bars, Mendeley Data, V1, 2020. https://dx.doi.org/10.17632/xx3zzj8xb2.1.
[19] J.P. Benthem, State of stress at the vertex of a quarter-infinite crack in a half-space, Int. J. Solids Struct. 13 (1977) 479–492, https://doi.org/10.1016/0020-7683(77)90042-7.
[20] J.P. Benthem, The quarter-infinite crack in a half space; Alternative and additional solutions, Int. J. Solids Struct. 16 (1980) 119–130, https://doi.org/10.1016/0020-7683(80)90029-3.
[21] M. Heyder, K. Kolk, G. Kuhn, Numerical and experimental investigations of the influence of corner singularities on 3D fatigue crack propagation, Eng. Fract. Mech. 72 (2005) 2095–2105, https://doi.org/10.1016/j.engfracmech.2005.01.006.
[22] J.C. Newman, I.S. Raju, An empirical stress-intensity factor equation for the surface crack, Eng. Fract. Mech. 15 (1981) 185–192, https://doi.org/10.1016/0013-7944(81)90116-8.
[23] S. Strobl, P. Supancic, T. Lube, R. Danzer, Surface crack in tension or in bending – a reassessment of the Newman and Raju formula in respect to fracture toughness measurements in brittle materials, J. Eur. Ceram. Soc. 32 (2012) 1491–1501, https://doi.org/10.1016/j.jeurceramsoc.2012.01.011.
[24] F. Yang, Z. Kuang, V.N. Shlyannikov, Fatigue crack growth for straight-fronted edge crack in a round bar, Int. J. Fatigue 28 (2006) 431–437, https://doi.org/10.1016/j.ijfatigue.2005.07.036.
[25] R.G. Chermahini, B. Palmberg, A.F. Blom, Fatigue crack growth and closure behaviour of semicircular and semi-elliptical surface flaws, Int. J. Fatigue 15 (1993) 259–263, https://doi.org/10.1016/0142-1123(93)90374-Y.
[26] C.-Y. Hou, Three-dimensional finite element analysis of fatigue crack closure behavior in surface flaws, Int. J. Fatigue 26 (2004) 1225–1239, https://doi.org/10.1016/j.ijfatigue.2004.02.007.
[27] C. Gardin, S. Fiordalisi, C. Sarrazin-Baudoux, M. Gueguen, J. Petit, Numerical prediction of crack front shape during fatigue propagation considering plasticity-induced crack closure, Int. J. Fatigue 88 (2016) 68–77, https://doi.org/10.1016/j.ijfatigue.2016.03.018.
[28] J. Newman Jr, I. Raju, Prediction of fatigue crack-growth patterns and lives in three-dimensional cracked bodies, in, Fracture 84, Elsevier (1984) 1597–1608.
[29] P.S. Song, Y.L. Shieh, Crack growth and closure behaviour of surface cracks, Int. J. Fatigue 26 (2004) 429–436, https://doi.org/10.1016/j.ijfatigue.2003.06.002.
[30] DNV, Offshore Standard DNVGL-OS-E302 "Offshore mooring chain", 2015.
[31] E.P. Zarandi, B.H. Skallerud, Experimental and numerical study of mooring chain residual stresses and implications for fatigue life, Int. J. Fatigue 135 (2020), 105530, https://doi.org/10.1016/j.ijfatigue.2020.105530.